Structure and coherency of bcc Nb precipitates in hcp Zr matrix from atomistic simulations

Zhengxuan Fan, Émile Maras, Maeva Cottura, Mihai-Cosmin Marinica, Emmanuel Clouet

Structure and coherency of bcc Nb precipitates in hcp Zr matrix from atomistic simulations

Zhengxuan Fan,[1] Émile Maras,[1] Maeva Cottura,[1,2]
Mihai-Cosmin Marinica,[1] and Emmanuel Clouet[1,*]

[1] *Université Paris-Saclay, CEA, Service de recherche en Corrosion et Comportement des Matériaux, SRMP, F-91191 Gif-sur-Yvette, France*

[2] *Université de Lorraine, CNRS, IJL, Nancy F-54000, France*

(Dated: November 7, 2024)

Abstract

We use atomistic simulations to study the structure and shape of niobium precipitates with a body-centered cubic crystallographic structure in a zirconium matrix with a hexagonal close-packed structure. We consider a Pitsch-Schrader orientation relationship, which is observed experimentally for Nb precipitates appearing under irradiation in zirconium alloys. In this regard, we have developed a Zr-Nb empirical potential using the embedded atom method. This parametrization offers a good description of the interfaces between Nb precipitates and the Zr matrix. The potential includes all the necessary physical ingredients to account for the coherency strain between both phases. The atomistic simulations reveal a significant decrease in the precipitates formation energy when they become semi-coherent, with enough misfit dislocations at the interface to eliminate the lattice misfit between the Nb precipitates and the Zr matrix. The "idealized" equilibrium shape that minimizes the formation energy of these semi-coherent precipitates matches the experimental shape: platelets lying in the Zr basal planes with a reduced dimension along the [0001] axis. Our simulations suggest that the platelet shape observed in zirconium for irradiation-induced Nb-enriched precipitates simply results from a minimization of their energy cost.

I. INTRODUCTION

The Zr-Nb binary system is a prototypical example of a demixing alloy, in which phase separation leads to the formation of two phases with different crystallographic structures, a Zr enriched hexagonal close-packed (hcp) α-phase and a Nb enriched body-centered cubic (bcc) β-phase. Used in the nuclear industry as a structural material, particularly for fuel cladding in nuclear power plants [1, 2], typical Zr-Nb alloys contain between 1 and 2.5 % Nb, *i.e.* a nominal concentration above the maximal solubility limit [3–5]. Consequently, these alloys form spherical β-Nb precipitates, with a typical size between 20 and 200 nm [6–9], embedded in an α-Zr matrix. These native β-Nb precipitates do not appear to have an orientation relationship with the matrix [8, 10] and are thus considered incoherent, although some specific orientation relationships (OR) have occasionally been reported [7, 11, 12]. Due to the low diffusivity of Nb in the α-Zr phase, equilibrium is not reached at the operating temperature, *i.e.* 300 - 350°C for the fuel cladding, resulting in a higher Nb concentration

* emmanuel.clouet@cea.fr; Corresponding author

in the α-Zr phase than the solubility limit. Under neutron irradiation, this supersaturated solid solution evolves, leading to the nucleation of a second population of β-Nb precipitates, which are smaller than the native ones [6, 8, 13–19]. These smaller precipitates form due to the accelerated precipitation kinetics induced by irradiation and remain stable when the alloy is annealed post-irradiation [20, 21].

In neutron-irradiated samples, the high density of $\langle a \rangle$ dislocation loops created by irradiation in the α-Zr matrix makes the irradiation-enhanced precipitates visible by transmission electron microscopy (TEM) only with a projected view in a prismatic plane using a $g = 0002$ diffracting vector, as this diffraction vector renders $\langle a \rangle$ loops invisible, thus allowing one to see the β-Nb precipitates. Under these imaging conditions, the nano-precipitates appear as needle-like particles, with their long dimension lying in the basal plane. Once the irradiation microstructure has been annealed and the $\langle a \rangle$ loops removed, precipitates can be imaged with different tilts and it becomes clear that they are actually platelets lying in the basal planes. Initially, they are almost circular with a $\sim 3\,\text{nm}$ diameter at low irradiation doses, but they become more acicular, elongated in the basal plane, at high irradiation doses [15]. The acicular precipitates exhibit a characteristic size of $6.5 \pm 3\,\text{nm}$ and $3.2 \pm 0.9\,\text{nm}$ in the basal plane, with a nearly random orientation of the long direction, and $1.4 \pm 0.4\,\text{nm}$ along the $[0001]_\alpha$ direction, resulting in a flattened needle shape [8]. TEM observations with energy dispersive X-ray spectroscopy (EDS) on neutron-irradiated Zr-Nb $M5_{\text{Framatome}}$[1] and ZIRLO® alloys, which have not been annealed post-irradiation, show the same shape and dimensions of the β-Nb particles [18, 22] as conventional TEM. These β-Nb precipitates, which appear during irradiation, have a significant influence on the properties of the Zr-Nb alloys. They contribute to hardening, even after post-irradiation annealing, as they remain stable [20, 21]. Through their equilibrium with the Nb in solid solution in the α-Zr phase, they affect the corrosion and hydriding resistance of Zr-Nb alloys [9, 23].

Similar β-Nb precipitates appear under proton irradiation [9, 23–26], although the length of the needles is usually larger ($\geq 20\,\text{nm}$ and up to $150\,\text{nm}$) than with neutron irradiation, or under electron irradiation [27]. Ion irradiation similarly leads to the formation of Nb-enriched nano-clusters, as observed with atom probe tomography (APT) by Matsukawa *et al.* [12, 17] in Zr-Nb alloys containing 1 % or 2.5 % Nb. In this case, the Nb clusters have

[1] M5 and $M5_{\text{Framatome}}$ are trademarks or registered trademarks of Framatome or its affiliates, in the USA or other countries.

a smaller mean diameter ($\sim 4\,\mathrm{nm}$). Although no TEM has been performed to confirm their crystallographic structure, it is reasonable to assume that they have the same bcc structure as the β-Nb particles that appear under neutron or proton irradiation. The flattened shape of these irradiation-induced β-Nb particles along the $[0001]_\alpha$ direction thus appears to be independent of the irradiation conditions.

As noted by Ribis *et al.* [8], the reason for the very thin thickness of the β-Nb precipitates along the $[0001]_\alpha$ direction is unknown. Sarce [28–30] has proposed that this shape results from the anisotropy of vacancies and interstitials diffusion. However, the proposed model, which neglects the impact of elastic stress fields on point defects diffusion, may be more relevant for fully incoherent precipitates than for the coherent or semi-coherent precipitates corresponding to the β-Nb particles appearing under irradiation [8, 23]. Irradiation-enhanced β-Nb precipitates have indeed an orientation relationship (OR) with the α-Zr matrix between the Pitsch-Schrader OR, $(0\bar{1}1)_\beta \parallel (0001)_\alpha$ and $[100]_\beta \parallel [2\bar{1}\bar{1}0]_\alpha$, and the Burgers OR, $(0\bar{1}1)_\beta \parallel (0001)_\alpha$ and $[111]_\beta \parallel [2\bar{1}\bar{1}0]_\alpha$. [8, 23]. These two ORs only deviate by a small rotation, $\sim 5.26°$ around the $[0001]_\alpha$ axis [31] and, as explained in [23], the OR of the β-Nb precipitates with the α-Zr matrix can generally be interpreted as a Pitsch-Schrader or a Burgers OR. This OR between the β-Nb precipitates and the α-Zr matrix necessarily impacts the shape of the precipitates, either through the energy cost of the corresponding interfaces or the elastic energy arising from the lattice misfit between both phases. In this article, we use atomistic simulations to determine if the observed shape of the β-Nb particles appearing under irradiation can be related to their formation energy. Our hypothesis is that the flattened needle shape, with a reduced size along the $[0001]_\alpha$ direction, minimizes the precipitate formation energy.

We first describe the energy models used to describe the Zr-Nb binary alloy at an atomic scale, considering *ab initio* calculations and a newly developed empirical potential to enable larger simulations. We then study infinite coherent interfaces between the β-Nb precipitates and the α-matrix, comparing results from *ab initio* calculations and our empirical potential. Finally, molecular statics simulations are performed to find the precipitate shape that minimizes its formation energy, considering both coherent and semi-coherent precipitates.

II. ENERGY MODELS

A. *Ab initio* calculations

Ab initio calculations are performed to complete the database used for fitting the empirical potential in the next subsection (§II B) and to determine interface energies (§III C). These calculations rely on the density functional theory DFT, using the VASP code [32]. The generalized gradient approximation (GGA) with Perdew-Burke-Ernzerhof parameterization [33] is used for the exchange and correlation functional. The interaction between core and valence electrons is modeled with the projector wave method, including 4s, 4p, 5s, and 4d electrons in valence states both for Zr and Nb and using a 370 eV cutoff energy for the plane-wave basis. The Brillouin zone is sampled with a Monkhorst-Pack grid with 24 k-points per inverse lattice parameter. The electronic density of states is integrated using Methfessel-Paxton broadening with a 0.2 eV smearing parameter. Atomic positions are relaxed until reaching a 10 meV Å^{-1} threshold on each Cartesian component of atomic forces, while keeping the periodicity vectors of the simulation cell fixed. As shown in tables I and II, these *ab initio* parameters lead to equilibrium lattice parameters and elastic constants in good agreement with experimental values for both hcp Zr and bcc Nb.[2]

Supercells used to calculate solution energies have been described in Ref. [5] and contains up to 250 atoms. For the simulation of infinite planar interfaces, we use supercells built from a stacking of β-Nb and α-Zr elementary cells containing each 4 atoms (*cf* definition of these elementary cells in Fig. 2, 3 and 4). These supercells contain up to 96 atoms for a stacking of 12 α-Zr and 12 β-Nb elementary cells.

B. Interatomic potential

We develop a new empirical potential to describe the binary Zr-Nb alloy using the embedded atom method (EAM). The aim of this potential is to conduct large-scale atomistic simulations of β-Nb precipitates embedded in an α-Zr matrix. To predict the elastic energy arising from the coherency constraint between the precipitate and the matrix, this potential

[2] *Ab initio* values are not given for the cohesive energies as these cohesive energies are notoriously hard to precisely define with DFT and as they are not necessary for the present study, the EAM potential being fitted on experimental cohesive energies.

TABLE I. Properties of the hcp phase of pure Zr predicted by the EAM potential (EAM #3 of Ref. [34]) and compared to DFT results and experimental data: cohesive energy E^{coh}, lattice parameter a and c, and elastic constants C_{ij} of the hcp phase.

	EAM	DFT	Experiments
E^{coh} (eV/atom)	6.635	/	6.32 [35]
a (Å)	3.234	3.235	3.232 [36]
c (Å)	5.168	5.179	5.182 [36]
C_{11} (GPa)	142	144	155.4 [37]
C_{33} (GPa)	168	164	172.5 [37]
C_{12} (GPa)	75	64	67.2 [37]
C_{13} (GPa)	76	66	64.6 [37]
C_{44} (GPa)	44	26	36.3 [37]
C_{66} (GPa)	33.5	40.	44.1 [37]

must accurately describe both the α-Zr and β-Nb phases, particularly their equilibrium lattice parameters and their elastic behavior. Additionally, a good description of the interfaces, including their structures and excess energies, between β-Nb precipitate and α-Zr matrix is required. As we intend to use this Zr-Nb potential in the near future to study the interaction of a dislocation gliding in the α-Zr matrix with β-Nb precipitates, the computational cost associated with this potential must be reasonable to enable molecular dynamics simulations on relevant timescales of several nanoseconds and for simulation cells containing typically one million atoms. Despite the rapid advancements in modern machine learning force fields, that offer interatomic interactions with $\mathcal{O}(N)$ scalability and near ab initio accuracy, significantly better than traditional force fields, they remain numerically intensive [42–45]. We choose instead to focus on the EAM formalism, which is well-suited to meet all our criteria, balancing accuracy and computational efficiency.

While no satisfactory EAM potential exists for the Zr-Nb binary system, Mendelev and Ackland [34] have developed three different EAM potentials for Zr. Among these potentials, EAM #3 is particularly well-suited to describe the α hcp phase, including dislocation properties controlling Zr plasticity [46–49]. Therefore, we employ this EAM #3 potential to describe pure Zr and only fit the pure Nb and the Zr-Nb alloying parts (*cf* appendix A).

TABLE II. Properties of pure Nb predicted by the EAM potential and compared to DFT results and experimental data. For the bcc phase: cohesive energy E^{coh}, lattice parameter a, elastic constants C_{ij}, vacancy and self-interstitial formation energy $E_{\mathrm{V}}^{\mathrm{form}}$ and $E_{\mathrm{SIA}}^{\mathrm{form}}$ (for the SIA, the $\langle 111\rangle$, $\langle 110\rangle$, and $\langle 100\rangle$ crowdions are considered, as well as the octahedral and tetrahedral positions). For the fcc and hcp phases: energy differences ΔE with respect to the bcc ground state and corresponding lattice parameters a and c.

	EAM	DFT	Experiments
E^{coh} (eV/atom)	7.57	/	7.57 [35]
a (Å)	3.304	3.308	3.303 [38]
C_{11} (GPa)	246.	242.	253. [39]
C_{12} (GPa)	133.	128.	133. [39]
C_{44} (GPa)	29.	31.	31. [39]
$E_{\mathrm{V}}^{\mathrm{form}}$ (eV)	2.71	2.7 [5]	2.6 ± 0.3 [40]
$E_{\mathrm{SIA}\langle 111\rangle}^{\mathrm{form}}$ (eV)	3.86	3.95 [41]	
$E_{\mathrm{SIA}\langle 110\rangle}^{\mathrm{form}}$ (eV)	4.09	4.31 [41]	
$E_{\mathrm{SIA}\langle 100\rangle}^{\mathrm{form}}$ (eV)	4.01	4.76 [41]	
$E_{\mathrm{SIAocta}}^{\mathrm{form}}$ (eV)	4.41	4.89 [41]	
$E_{\mathrm{SIAtetra}}^{\mathrm{form}}$ (eV)	4.27	4.56 [41]	
ΔE_{fcc} (meV/atom)	184.	324. [41]	
a_{fcc} (Å)	4.02	4.217 [41]	
ΔE_{hcp} (meV/atom)	215.	297. [41]	
a_{hcp} (Å)	2.83	2.867 [41]	
c_{hcp} (Å)	4.76	5.238 [41]	

The fitting of the potential is performed using the same procedure as the one described in Ref. [50]. The pure Nb part is fitted on configurations corresponding to the perfect bcc, fcc and hcp crystal structures (equilibrium lattice parameters and relative energies), the elastic constants of the bcc crystal and its $E(V)$ equation of state in a $\pm 4\%$ variation range of the lattice parameter. The formation energies of the vacancy and different configurations of the self interstitial atom (SIA) in the bcc phase are also considered. Table II shows that

TABLE III. Properties of Zr-Nb binary alloy. Solution energies of Nb in α-Zr phase $\Omega^{\alpha}_{\rm mix}$ and Zr in β-Nb phase $\Omega^{\beta}_{\rm mix}$. Interface energies $\Gamma^{\alpha/\beta}_{n}$ for different orientations $\vec{n}$ of the interface plane: $\vec{n} = \vec{x} \parallel [2\bar{1}\bar{1}0]_\alpha \parallel [100]_\beta$; $\vec{n} = \vec{y} \parallel [01\bar{1}0]_\alpha \parallel [011]_\beta$ with interfaces I, II, III corresponding to stable faults identified on the different possible cut-planes (*cf* Fig. 4); $\vec{n} = \vec{z} \parallel [0001]_\alpha \parallel [0\bar{1}1]_\beta$ with interfaces ABC and ABA corresponding to the different possible stacking of the fault (*cf* Fig. 3). For $\Gamma^{\alpha/\beta}_{x}$, values in italic are obtained by relaxing atoms only in the $\vec{x}$ direction i.e. perpendicular to the interface plane (*cf* §III C).

	EAM	DFT
$\Omega^{\alpha}_{\rm mix}$ (eV)	0.480	0.632 [5]
$\Omega^{\beta}_{\rm mix}$ (eV)	0.477	0.312 [5]
$\Gamma^{\alpha/\beta}_{x}$ (meV Å^{-2})	*29.2*	8.5 (*27.4*)
$\Gamma^{\alpha/\beta}_{y\,\rm I}$ (meV Å^{-2})	30.5	20.8
$\Gamma^{\alpha/\beta}_{y\,\rm II}$ (meV Å^{-2})	78.0	91.2
$\Gamma^{\alpha/\beta}_{y\,\rm III}$ (meV Å^{-2})	20.5	11.7
$\Gamma^{\alpha/\beta}_{z\,\rm ABC}$ (meV Å^{-2})	17.2	unstable
$\Gamma^{\alpha/\beta}_{z\,\rm ABA}$ (meV Å^{-2})	20.1	8.7

the obtained EAM potential gives a good description of pure Nb. This potential correctly predicts the bcc phase as the most stable one and agrees well with *ab initio* calculations and experiments for the fundamental properties of this bcc phase, in particular its equilibrium lattice parameter and elastic constants. Table II shows that this EAM potential nevertheless underestimates the energy difference of other crystallographic structures with respect to the bcc ground state. In particular, the potential leads to an energy of the hcp phase, $\Delta E_{\rm hcp} = 215\,$meV/atom, lower than the one obtained by *ab initio* calculations (297 meV/atom). One thus expects that this potential will overestimate the energy barrier opposing the nucleation of a bcc Nb embryo in an hcp matrix, while still giving a reasonable description of the physical mechanisms. As we only consider Nb precipitates, which already have a bcc crystallographic structure, such a deficiency of the potential should be harmless for the present study. To improve the potential and give a better description of the relative energies of the different crystallographic structures, it would be necessary to go beyond the EAM formalism and to include an angular dependence of atomic bonding, an important ingredient in a transition

metal like Nb. But this will be at the detriment of the numerical cost.

The Zr-Nb part is fitted on impurity calculations, *i.e.* a Nb solute atom in a hcp Zr matrix and an Zr solute atom in a bcc Nb matrix, considering four different simulation cells, thus four different solute concentrations in each case. Melted alloys using six different configurations with compositions ranging between 1/3 and 2/3 are also employed. Atomic forces and structure energies of these different configurations are used in the cost function of the fitting algorithms. Configurations used to model stable β-Nb/α-Zr interfaces (see next section §III) are also included in the database to ensure that the potential correctly describes interfaces between the precipitates and the matrix. As shown in table III, the potential correctly predicts positive solution energies $\Omega^{\alpha}_{\text{mix}}$ and $\Omega^{\beta}_{\text{mix}}$ both for a Nb solute atom in hcp Zr and for a Zr solute atom in bcc Nb, thus correctly describing the binary Zr-Nb system as an unmixing alloy. The energetic description of the alloy is nevertheless not fully quantitative as values obtained with this EAM potential for solution energies significantly differ from *ab initio* values and the potential fails to reproduce the asymmetry of these solution energies. From a thermodynamic point of view, this potential should be rather considered as prototypical of a phase separating alloy like Zr-Nb, *i.e.* a binary system with an unmixing tendency leading to the formation of an α and a β phase having properties of α-Zr and β-Nb, rather than a real quantitative description of this binary alloy. The potential also leads to interface energies in reasonable agreement with *ab initio* values for the different orientations studied, as described in the next section, correctly predicting the energy hierarchy for the different configurations of the $\vec{y} \parallel [01\bar{1}0]_{\alpha}$ orientation for instance. These interface energies are nevertheless slightly too high compared to *ab initio* values. Atomic simulations performed with this potential will therefore give more weight than they should to these coherent interfaces. Despite this overestimation, we will see in the last section that this is the elastic energy, and not the energy cost of the interfaces, which controls the equilibrium shape of the β-Nb precipitates when they remain coherent with the α-Zr matrix.

The analytical functions and parameters corresponding to this Zr-Nb EAM potential are given in appendix A.

III. INFINITE INTERFACES

We first study the structure and the energy of infinite interfaces between α-Zr and β-Nb corresponding to Pitsch-Schrader orientations between both phases. Specifically, the orientation of the reference axis and the corresponding periodicity lengths of the α and β crystal structure are:

- $\vec{x} \parallel 1/3\,[2\bar{1}\bar{1}0]_\alpha \parallel [100]_\beta$ with $\lambda^x_\alpha = a_{\mathrm{Zr}} = 3.234\,\text{Å}$ and $\lambda^x_\beta = a_{\mathrm{Nb}} = 3.304\,\text{Å}$;
- $\vec{y} \parallel [01\bar{1}0]_\alpha \parallel [011]_\beta$ with $\lambda^y_\alpha = a_{\mathrm{Zr}}\sqrt{3} = 5.601\,\text{Å}$ and $\lambda^y_\beta = a_{\mathrm{Nb}}\sqrt{2} = 4.673\,\text{Å}$;
- $\vec{z} \parallel [0001]_\alpha \parallel [0\bar{1}1]_\beta$ with $\lambda^z_\alpha = c_{\mathrm{Zr}} = 5.167\,\text{Å}$ and $\lambda^z_\beta = a_{\mathrm{Nb}}\sqrt{2} = 4.673\,\text{Å}$.

The lattice mismatch between the two phases results in significant coherency strains. For illustration, if we assume that the α phase remains unstrained and all the deformation occurs in the β phase, the β phase coherency strain in direction $\vec{u}$ is given by $\varepsilon^\beta_{uu} = (\lambda^u_\alpha - \lambda^u_\beta)/\lambda^u_\beta$, leading to $\varepsilon^\beta_{xx} = -2.1\,\%$, $\varepsilon^\beta_{yy} = 19.9\,\%$, and $\varepsilon^\beta_{zz} = 10.6\,\%$. Although this coherency strains are reduced by partitioning between both phases, they remain substantial. Consequently, the calculation of interface energy requires special care, as described below, to withdraw any contribution from the elastic energy.

A. Methods

Infinite interfaces are modeled using simulation cells with periodic boundary conditions in all directions. A block of perfect α-Zr crystal and a block of perfect β-Nb are first prepared, orientated correctly to create an interface with a normal vector $\vec{n}$ (step 1 in Fig. 1). Each block is then strained to eliminate the lattice mismatch between both phases at the interface plane, resulting in the same interface area $S_{\vec{n}}$ in both phases (step 2 in Fig. 1). The homogeneous strains ε^α and ε^β are chosen to minimize the elastic energy of the sandwich structure according to linear elasticity (*cf* appendix B). The two blocks are then joined to create a periodic cell defined by vectors $\vec{u}_1$, $\vec{u}_2$, and $\vec{u}_3$ (steps 3 in Fig. 1). In addition, the blocks are displaced by a relative vector $\vec{f}$ within the interface plane, and the periodicity vector $\vec{u}_3$, initially normal to the interface plane, is modified to $\vec{u}_3 + 2\vec{f}$ to ensure the same atomic configuration for the two interfaces present in the simulation cell (step 4 in Fig. 1). Finally, the sandwich structure is relaxed with atomic simulations, allowing

atomic relaxations only in the direction $\vec{n}$ perpendicular to the interface plane to prevent the disappearance of the fault introduced in the interface plane during relaxation. The interface energy is thus obtained as a function of the fault vector $\vec{f}$. The simulation approach is similar to the one used in single-phase crystals to define generalized stacking fault energies [51, 52].

The interface energy is defined by

$$\Gamma_{\vec{n}}^{\alpha/\beta} = \frac{E\left[\mathrm{Zr}_n\mathrm{Nb}_m\right] - E\left[\mathrm{Zr}_n\right] - E\left[\mathrm{Nb}_m\right]}{2S_{\vec{n}}}, \tag{1}$$

where $E\left[\mathrm{Zr}_n\mathrm{Nb}_m\right]$ is the energy of the periodic supercell containing the interface with n Zr and m Nb atoms, while $E\left[\mathrm{Zr}_n\right]$ and $E\left[\mathrm{Nb}_m\right]$ are the reference energies of the pure α-Zr and β-Nb phases for the same number of atoms and the same applied strain as in the initial sandwich structure. The factor 2 in Eq. 1 arises from the presence of two interfaces in the periodic supercell, each covering an area $S_{\vec{n}}$. Generalized interface energies are obtained by plotting the interface energy as a function of the fault vector. Minima appearing on the 2D surface defined by this function $\Gamma_{\vec{n}}^{\alpha/\beta}(\vec{f})$ indicate possible stable configurations of the interface.

These stable configurations are then simulated in simulation boxes with different periodicity lengths h_3 in the direction $\vec{n}$ normal to the interface, keeping the phase ratio $n_{\mathrm{Zr}}/n_{\mathrm{Nb}} = n/m$ constant, where n_{Zr} and n_{Nb} are the number of α-Zr and β-Nb elementary

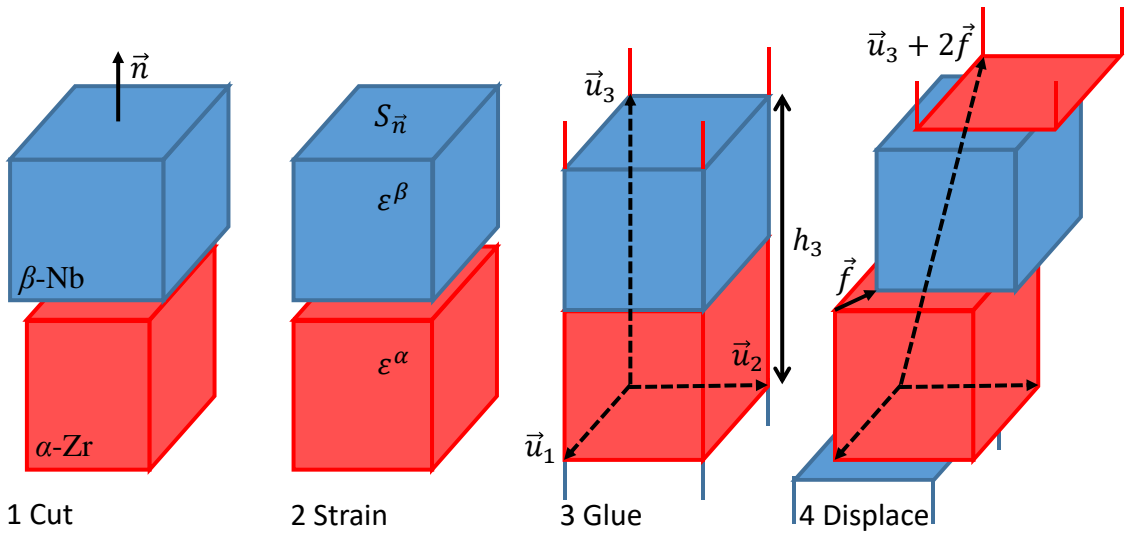

FIG. 1. Sketch describing the different steps used to create an infinite interface of normal $\vec{n}$ between α-Zr and β-Nb phases in a periodic simulation cell.

cells stacked in the α and β blocks composing the periodic sandwich structure. Although most of the elastic contribution to the excess energy has been already excluded in the definition of the interface energy (Eq. 1), there may be a remaining elastic contribution leading to a linear variation of the interface energy with the periodicity length h_3. This elastic contribution can be eliminated by considering the value of $\Gamma_{\vec{n}}^{\alpha/\beta}$ in the vanishing limit $h_3 \to 0$, while keeping the phase ratio $n_{\mathrm{Zr}}/n_{\mathrm{Nb}}$ constant [53, 54].

B. Generalized interface energies

Generalized interface energies are calculated with the EAM potential for the three interfaces of normal $\vec{u}_3$ parallel to $\vec{x}$, $\vec{y}$ and $\vec{z}$. Results are presented in Figs. 2, 3 and 4, with the crystallographic definition of the elementary α-Zr and β-Nb phases appearing on the right. All calculations have been performed with a phase ratio $n_{\mathrm{Zr}}/n_{\mathrm{Nb}} = 1$, using a stacking of 6 α-Zr and 6 β-Nb elementary cells.

Only one minimum exists for the interface of normal $\vec{x}$ (Fig. 2). It corresponds to a

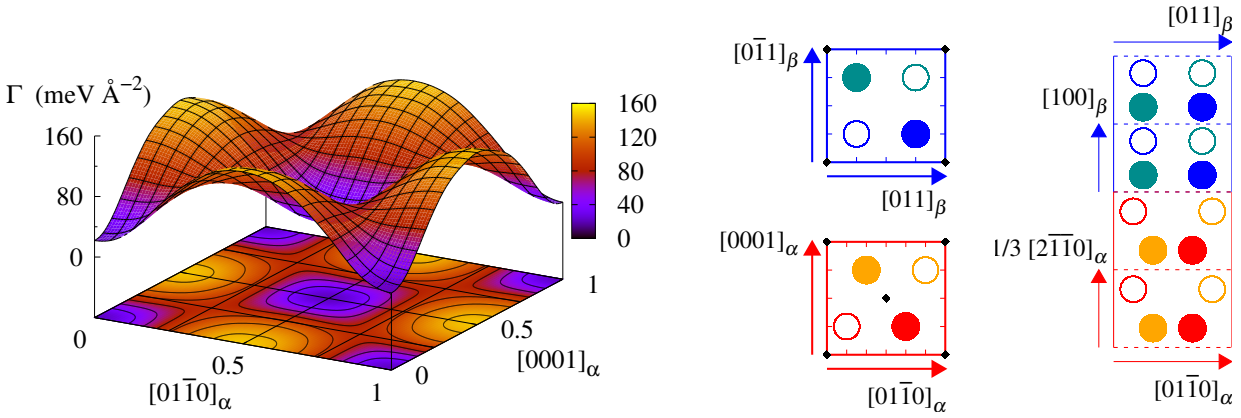

FIG. 2. Generalized interface energy for an interface of normal $\vec{x} \parallel 1/3\,[2\bar{1}\bar{1}0]_\alpha \parallel [100]_\beta$. The interface energy $\Gamma_{\vec{x}}^{\alpha/\beta}$ is presented as a function of the fault vector $\vec{f}$ on the left, while the crystallographic structures of the α-Zr (red and orange drawing) and β-Nb phases (blue and cyan drawing) are sketched on the right for two different projection directions. Zr and Nb atoms are drawn as circles and the elementary cells are depicted with continuous and dashed lines. The positions of the minima appearing on the 2D surface defined by $\Gamma_{\vec{x}}^{\alpha/\beta}$ are shown by black symbols on the projections in the interface plane: this corresponds to the origin of the elementary cell in the β-Nb phase and to the same position shifted by the fault vector $\vec{f}$ in the α-Zr phase.

configuration which maximizes the distance between neighboring Zr and Nb atoms at the interface. On the other hand, two minima can be found for the interface of normal $\vec{z}$ (Fig. 3). In this orientation, the interface is parallel to the basal planes of the α-Zr phase. The hcp structure can be defined by an $ABAB$ stacking of basal planes along the [0001] direction. One minimum corresponds to a configuration where the Nb layer lies at the interface in an A position, thus following the hcp network, while in the other minimum configuration the Nb atoms lie at the interface in the hollow C sites of the hcp basal planes, leading to an ABC stacking, *i.e.* a stacking corresponding locally to a face-centered cubic (FCC) structure. We will differentiate these two possible configurations of the $\vec{z}$ interface by naming them ABA and ABC.

The situation is more complex for the interface with normal $\vec{y}$, as the $\{01\bar{1}0\}$ prismatic planes of the α-Zr phase parallel to the interface are corrugated. Therefore, there are two different positions where the interface plane can be located in the α-Zr phase, leading to the types I and II interfaces shown in Fig. 4. In addition to these two different configurations,

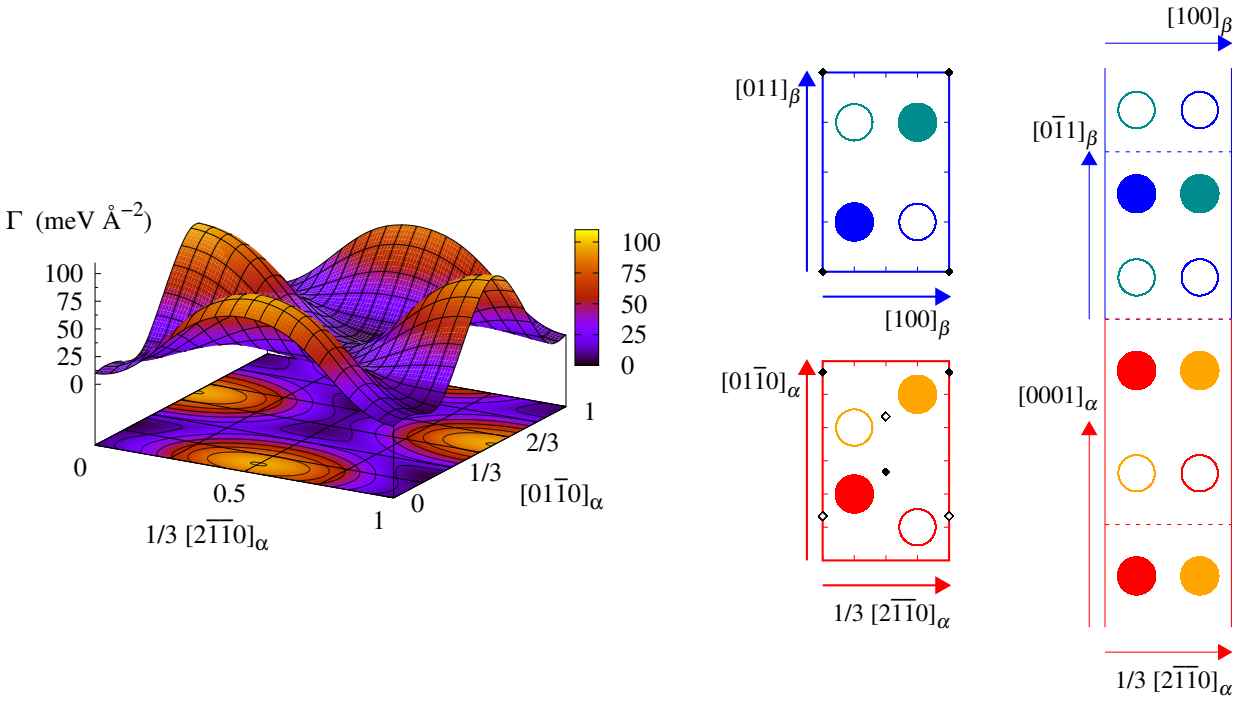

FIG. 3. Generalized interface energy for an interface of normal $\vec{z} \parallel [0001]_\alpha \parallel [0\bar{1}1]_\beta$. The positions of the minima corresponding to an ABA and an ABC stacking are indicated by respectively filled and empty black diamonds on the Nb and Zr unit cells projections.

we consider a third one (type III) where the interface plane is a mixture of Zr and Nb atoms. Each of these three possible $\vec{y}$ interfaces leads to only one minimum.

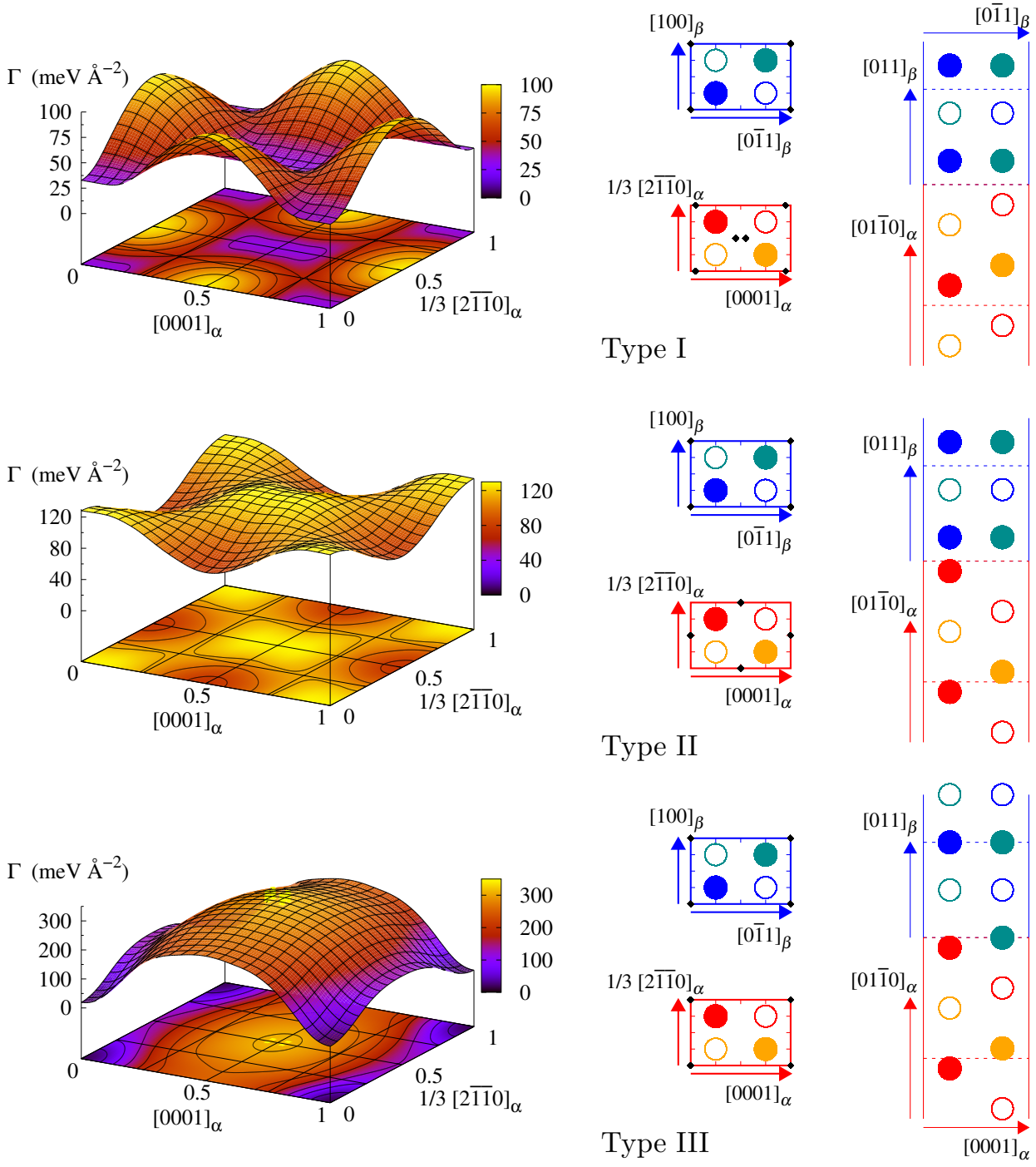

FIG. 4. Generalized interface energy for an interfaces of normal $\vec{y} \parallel [01\bar{1}0]_\alpha \parallel [011]_\beta$.

C. Interface energies

We now compute the interface energies for different periodicity lengths h_3, keeping the phase ratio $n_{\mathrm{Zr}}/n_{\mathrm{Nb}} = 1$, for the different minima previously identified on the generalized interface energies. Calculations are performed with the EAM potential, first allowing atomic relaxations only in the direction $\vec{n}$ normal to the interface plane, and then with full atomic relaxations. For the interface of normal $\vec{x}$, full relaxations were not possible due to the large lattice misfits. As a result, the homogenous strains ε^{α} and ε^{β} applied to both phases are high, and when the structure is fully relaxed, depending on the phase ratio and periodicity length h_3, at least one of the two phases does not maintain its initial α or β crystallographic structure. Therefore, only results with relaxations constrained to the direction perpendicular to the interface are considered for this $\vec{x}$ orientation. For the other two orientations, $\vec{y}$ and $\vec{z}$, full relaxations have only a marginal impact on the obtained interface energies compared to constrained relaxations (see the difference between empty and filled symbols in Fig. 5a-c).

As expected, we observe a linear variation of the interface energies with the periodicity length h_3 for all interfaces (Fig. 5a-c). The slope of this linear variation is negative, indicating that our definition of the interface energy (Eq. 1) slightly overestimates the elastic energy. This is expected as the position of the interface plane can shift during atomic relaxation, allowing a further reduction of the elastic energy compared to the initial guess based on linear elasticity theory. In all cases, a clear extrapolation of the interface energy in the limiting case $h_3 \to 0$ can be defined, leading to the interface energies shown in table III.

The same interfaces have been modeled with *ab initio* calculations, maintaining the phase ratio $n_{\mathrm{Zr}}/n_{\mathrm{Nb}} = 1$, leading to the interface energies shown in Fig. 5d-f. As with the EAM potential, a linear variation of the interface energy as a function of the periodicity length h_3 is observed, allowing a clear definition of the interface energy $\Gamma_{\vec{n}}^{\alpha/\beta}$ free of any elastic contribution in the limit $h_3 \to 0$.

For the interface of normal $\vec{x}$ (Fig. 5d), calculations have been performed with relaxation of the atomic positions only in the direction perpendicular to the interface plane and also with full relaxation, as the instability of strained phases, which we have encountered for this orientation with the EAM potential, did not appear with *ab initio*. Partial relaxation leads to very close values of the interface energy: $\Gamma_{x}^{\alpha/\beta} = 27.4\,\mathrm{meV\,\AA^{-2}}$ for *ab initio* and $29.2\,\mathrm{meV\,\AA^{-2}}$ for EAM. Full relaxation in *ab initio* calculations leads to a lower value ($8.5\,\mathrm{meV\,\AA^{-2}}$).

Although the fully relaxed structure can still be identified as an interface between an α and a β phase, the crystals, in particular the hcp lattice, are severely distorted by the large lattice misfit imposed by the coherent interface for this $\vec{x}$ orientation. Strong anharmonicity of the lattice elastic response is therefore expected.

For the interface of normal $\vec{y}$, the same hierarchy between the different interface types is observed with *ab initio* and EAM (Figs. 5b and e). Both energy models predict that the type III interface has the lowest energy, while the type II interface has a much higher energy than the other two configurations. Interface energies obtained with *ab initio* calculations are lower than with the EAM potential (11.7 *vs* 20.5 meV Å^{-2} for type III), but the energy difference remains reasonable.

For the interface of normal $\vec{z}$, only the ABA configuration has been found stable in *ab initio* calculations, leading to $\Gamma^{\alpha/\beta}_{z\,\mathrm{ABA}} = 8.7\,\mathrm{meV\,\AA^{-2}}$. Starting from an ABC configuration for the interface, full atomic relaxation leads to an interface having locally the same ABA configuration with an additional homogeneous strain spreading across the whole simulation cell to comply with the constraint imposed by periodicity. This contrasts with the results of EAM, where both configurations have been found stable, with the ABC configuration having a lower energy than ABA, 17.2 *vs* 20.1 meV Å^{-2}. Higher interface energies are also obtained for this $\vec{z}$ interface orientation with the EAM potential than with *ab initio* calculations, although the difference remains acceptable.

With values varying between 20.1 and 29.2 meV Å^{-2} for the lowest interface energies found for the different interface orientations (Table III), the Zr-Nb EAM potential provides a reasonable description of the Zr-Nb interfaces. It slightly overestimates the energy cost of these interfaces, as *ab initio* calculations predict lower interface energies (between 8.7 and 11.7 meV Å^{-2} for the most stable configurations), with the error remaining acceptable. Moreover, both energy models agree on the weak anisotropy of the interface energy. Hence, this EAM potential appears appropriate for providing a qualitative description of interfaces within this binary system.

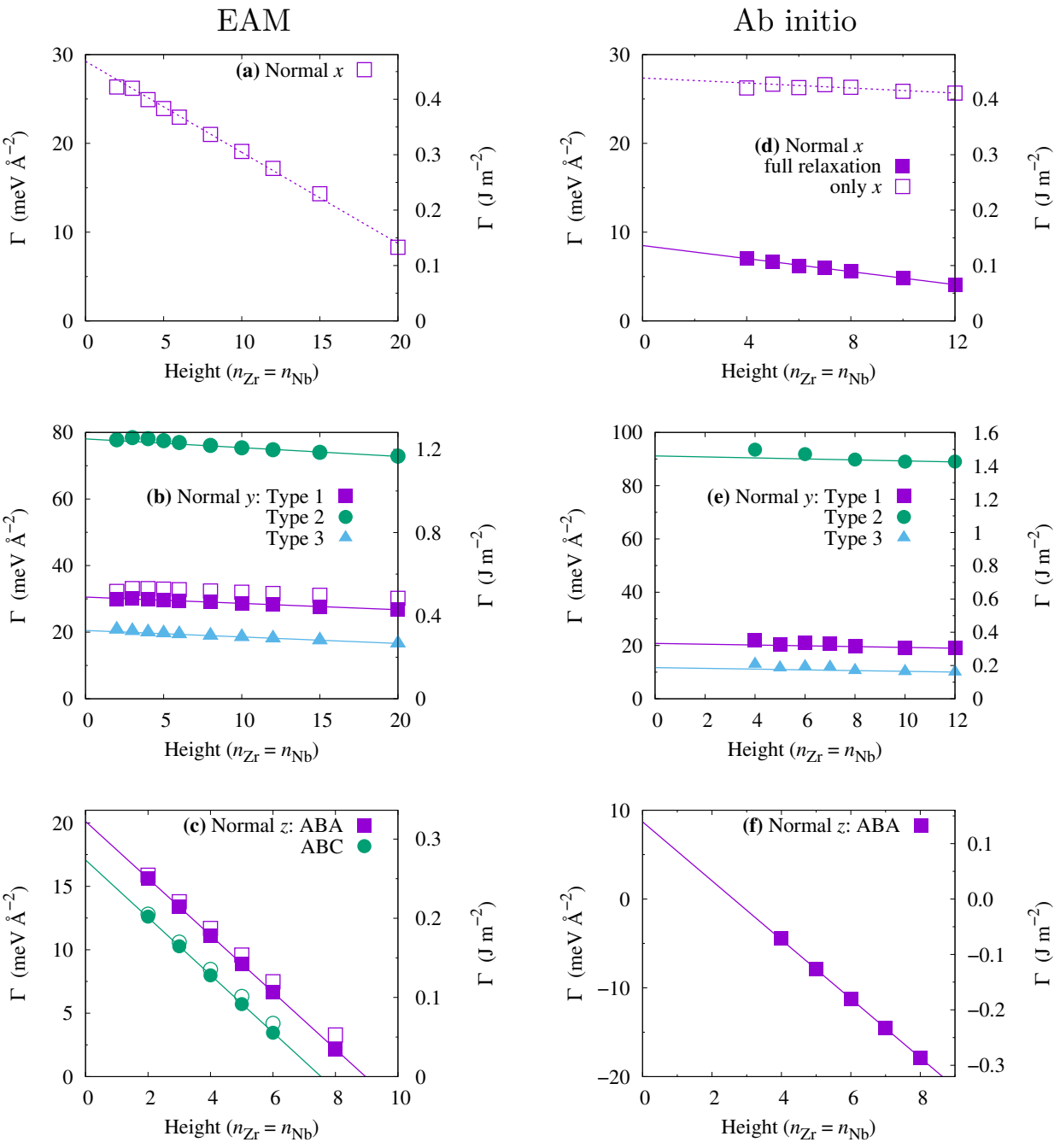

FIG. 5. Variation of the interface energy with the number of stacked planes, *i.e.* the periodicity length h_3, for the three different orientations of the interface plane and the different minima identified on the generalized interface energies. Filled and empty symbols are for simulations where atomic positions have been relaxed respectively in all directions (EAM, only for $\vec{y}$ and $\vec{z}$ interfaces) or only in the direction perpendicular to the interface plane. Subfigures on the left (a-c) and right (d-f) columns are respectively for EAM and *ab initio* calculations.

IV. NIOBIUM PRECIPITATES

We now study the formation energy of a niobium precipitate with a fixed volume but varying shape, embedded in a zirconium matrix, using the Zr-Nb EAM potential with a Pitsch-Schrader orientation. Our goal is to determine the precipitate shape that minimizes the formation energy and compare it to the shape observed experimentally by TEM. We consider both fully coherent precipitates (without misfit dislocations) and semi-coherent precipitates (with misfit dislocations) with simplified parallelepiped shapes.

A. Methods

The precipitate contains 4800 Nb atoms, corresponding to a volume equal to $86.5\,\mathrm{nm}^3$ in its unstrained state, closely matching the volume of precipitates observed in experiments. The simulation box dimensions are $108\,\lambda_x^\alpha = 349\,\text{Å}$, $62\,\lambda_y^\alpha = 347\,\text{Å}$, and $68\,\lambda_z^\alpha = 351\,\text{Å}$ in the directions $\vec{x} \parallel 1/3\,[2\overline{1}\overline{1}0]_\alpha$, $\vec{y} \parallel [01\overline{1}0]_\alpha$, and $\vec{z} \parallel [0001]_\alpha$, respectively, containing over 1.8 million atoms.

We generate different precipitate shapes, all parallelepipeds with sides of normal $\vec{x}$, $\vec{y}$ and $\vec{z}$ but with varying aspect ratios, and thus varying sizes l_x, l_y, and l_z in each direction, keeping the precipitate volume $V = l_x\,l_y\,l_z$ constant. Only precipitate shapes with a size larger than 10 Å in all directions are considered. Coherent precipitates are created by removing the same number of Zr atoms in the matrix and inserting the precipitate in the cavity after an homogeneous strain has been applied to cancel the lattice misfit between the precipitate and the matrix. The precipitate is slightly compressed in the $\vec{x}$ direction and significantly dilated in $\vec{y}$ and $\vec{z}$ directions. Atomic positions are then relaxed while keeping the periodicity vectors of the simulation box constant. Finally, the precipitate formation energy is defined as

$$\Delta E = E[\mathrm{Zr}_n\mathrm{Nb}_m] - nE_{\mathrm{Zr}}^{\mathrm{coh}} - mE_{\mathrm{Nb}}^{\mathrm{coh}},$$

where n and m are the number of Zr and Nb atoms ($m = 4800$ and $n{+}m = 4{\times}108{\times}62{\times}68$ for a coherent precipitate) and $E_{\mathrm{Zr}}^{\mathrm{coh}}$ and $E_{\mathrm{Nb}}^{\mathrm{coh}}$ are the cohesive energies of Zr and Nb, respectively.

We also study semi-coherent precipitates by introducing n_{D}^u misfit dislocations at the precipitate/matrix interfaces to accommodate the lattice misfit in the $\vec{e}_u$ direction, initially considering $u = y$, which leads to the largest misfit. This is done by keeping fixed the

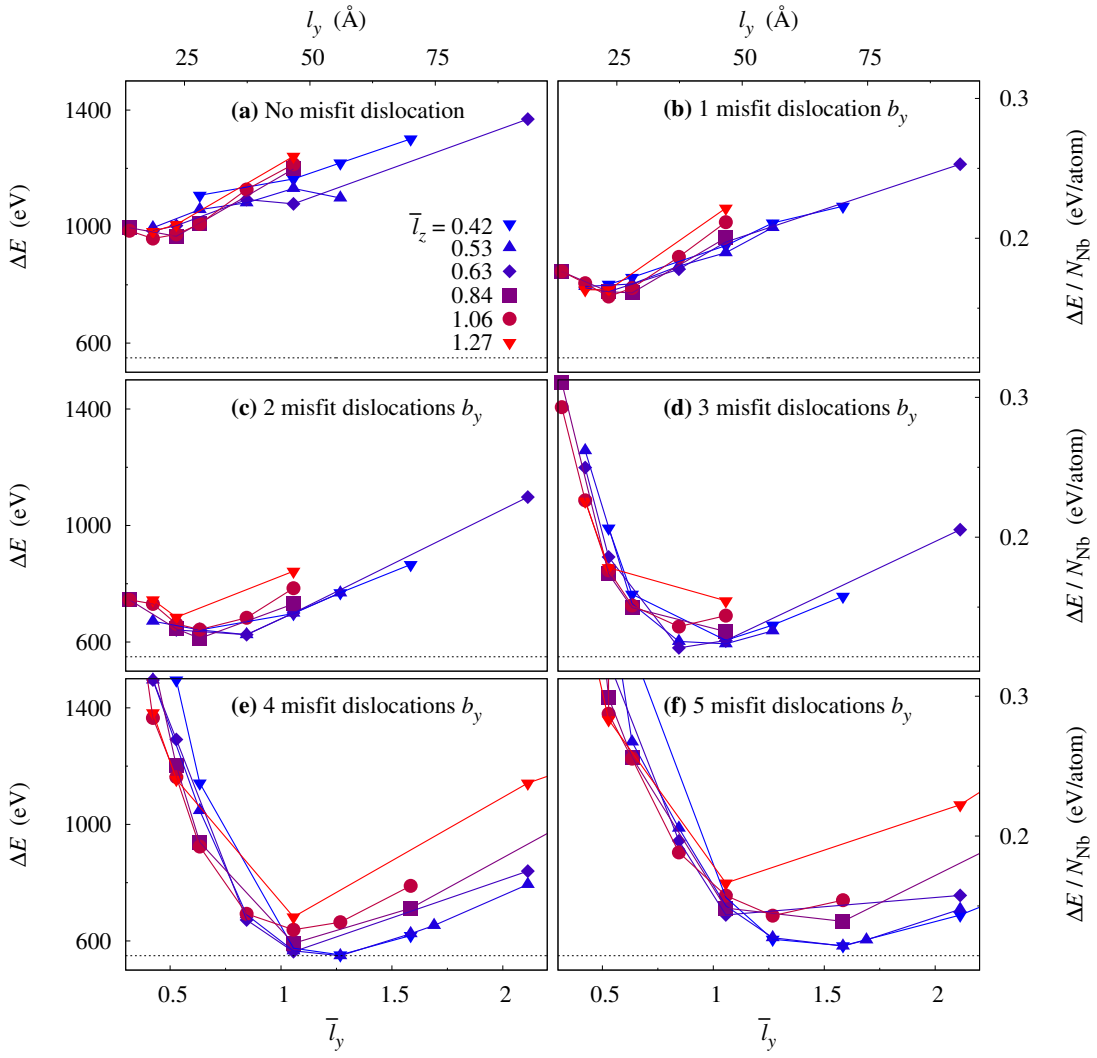

FIG. 6. Formation energy of a niobium precipitate of fixed volume V as a function of its elongation $\bar{l}_y = l_y/\sqrt[3]{V}$ (or length l_y) in the y direction and for different elongations $\bar{l}_z = l_z/\sqrt[3]{V}$ in the z direction. The precipitate is fully coherent in (a) or contains different numbers of misfit dislocations in (b)-(f) to accommodate the lattice misfit in the y direction. The horizontal dotted line correspond to the minimum formation energy.

number of Nb atoms in the precipitate ($m = 4800$) and removing in the α matrix the Zr atoms belonging to n^u_{D} planes of normal $\vec{e}_u$, which intersect the precipitate. This Volterra procedure creates n^u_{D} pure prismatic dislocation loops of Burgers vector $\vec{b}_u = \lambda^u_\alpha/2\,\vec{e}_u$ around the precipitate at the interface with the matrix, as there are 2 planes per periodicity length λ^u_α. These prismatic loops are interstitial in nature, as the density of the atomic planes is denser in the precipitate than in the matrix, and atoms have been removed in the matrix

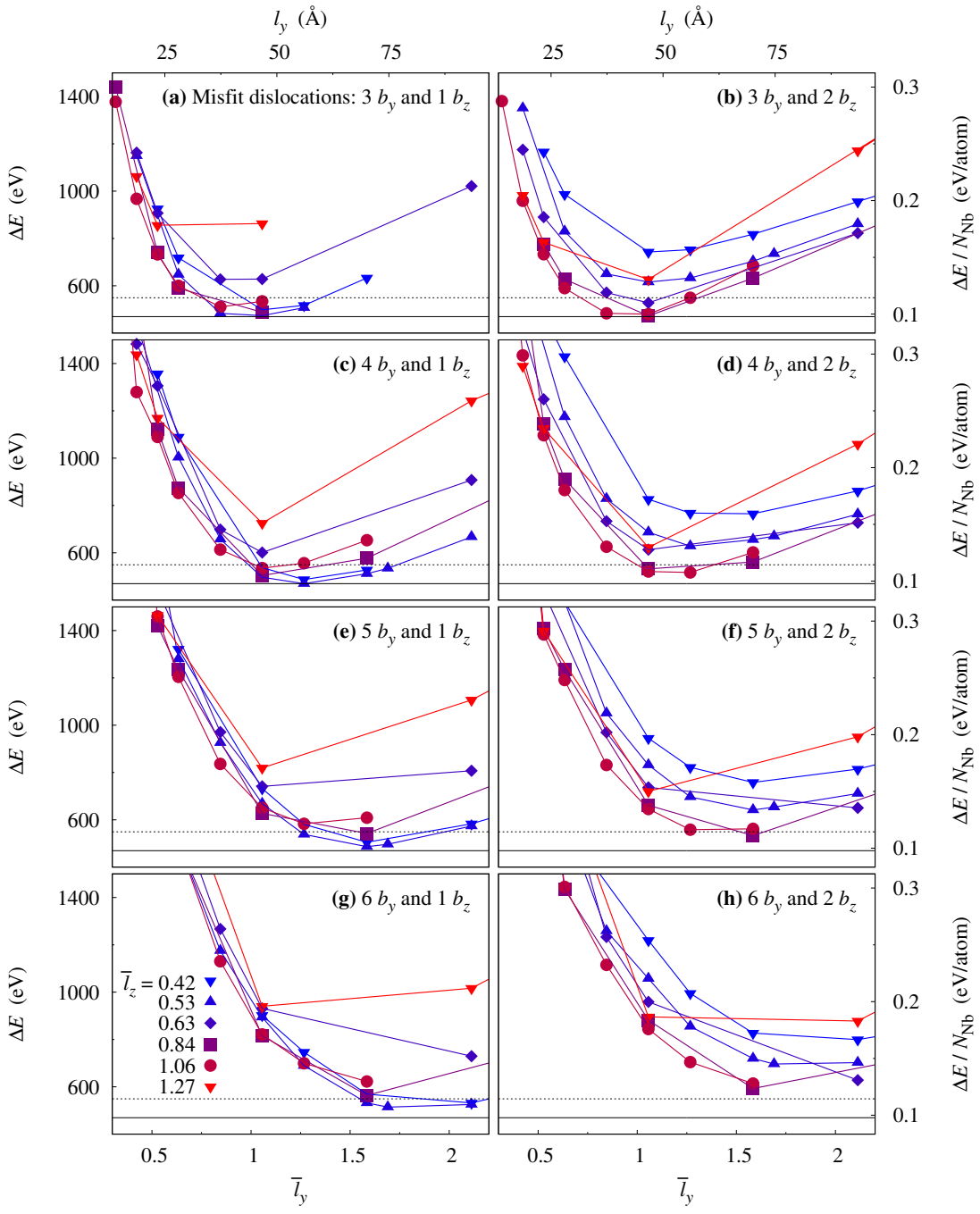

FIG. 7. Formation energy of a niobium precipitate of fixed volume V as a function of its elongation $\bar{l}_y = l_y/\sqrt[3]{V}$ (or length l_y) in the y direction and for different elongations $\bar{l}_z = l_z/\sqrt[3]{V}$ in the z direction. The precipitate contains different numbers of misfit dislocations to accommodate the lattice misfit in the y and the z directions. The horizontal dotted and solid lines correspond to the minimum formation energies, respectively without and with b_z misfit dislocations.

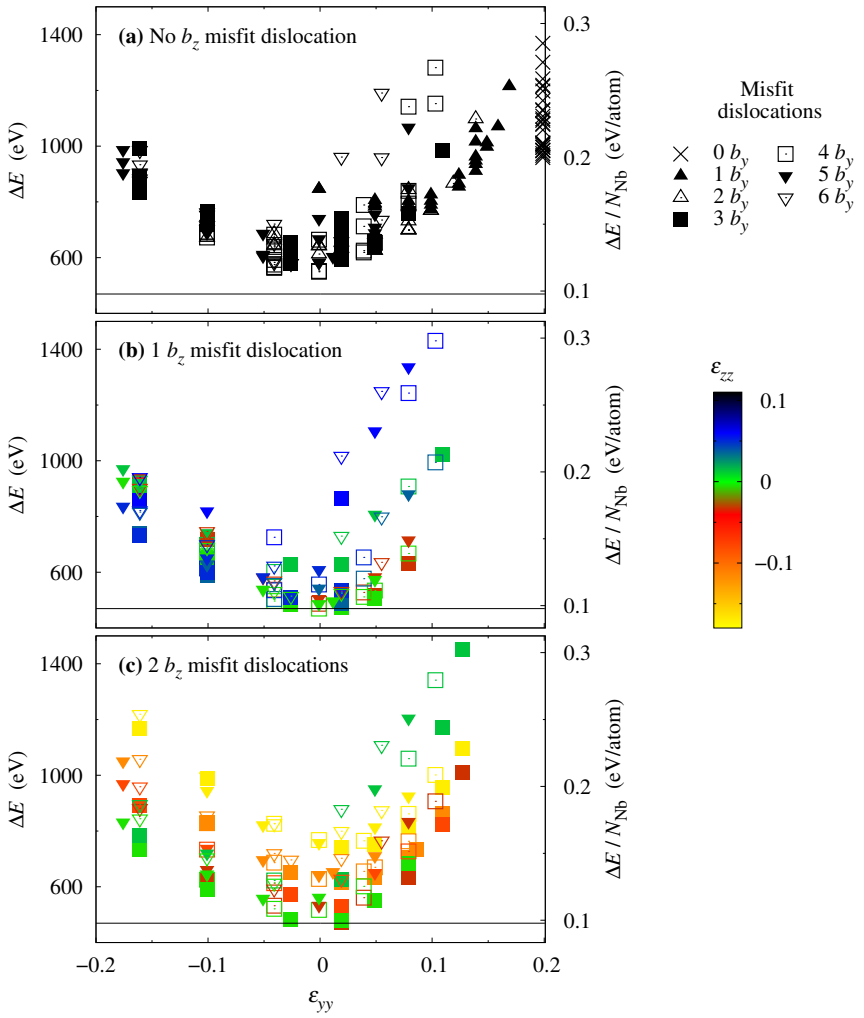

FIG. 8. Formation energy of a niobium precipitate of fixed volume V as a function of its eigenstrain ε_{yy} (abscissa coordinate) and ε_{zz} (color map) for different number of misfit dislocations (Eq. 2).

to compensate for the smallest atomic volume of the β-Nb phase than the one of the α-Zr phase. This Volterra procedure is therefore equivalent to the absorption of interstitial atoms by the precipitate to compensate for the different atomic volumes of the α and β phases. The eigenstrain necessary to embed the precipitate in the matrix before relaxation becomes

$$\varepsilon^{\beta}_{uu} = \frac{(n^u_\beta - n^u_{\mathrm{D}}/2)\lambda^u_\alpha - n^u_\beta \lambda^u_\beta}{n^u_\beta \lambda^u_\beta}, \tag{2}$$

where n^u_β is the number of β-phase planes in the precipitate in the $\vec{e}_u$ direction and $l_u = n^u_\beta \lambda^u_\beta$ is the corresponding initial length of the precipitate. In the absence of misfit dislocations ($n^u_{\mathrm{D}} = 0$), the eigenstrain equals those given at the beginning of section III for fully coherent

precipitates.

B. Formation energy and aspect ratio

For coherent precipitates, Fig. 6(a) shows that the minimum formation energy is achieved when the precipitates have a very small size in the $\vec{y} \parallel [01\bar{1}0]_\alpha$ direction: it occurs for the reduced sizes $\bar{l}_x = l_x/\sqrt[3]{V} = 2.2$, $\bar{l}_y = 0.42$ and $\bar{l}_z = 1.1$, which corresponds to $l_x = 9.9$, $l_y = 1.9$ and $l_z = 4.7\,\text{nm}$ for the precipitate volume considered here. Thus, coherent precipitates with minimum formation energy are elongated in the $\vec{x} \parallel [2\bar{1}\bar{1}0]_\alpha$ direction and small in the $\vec{y} \parallel [01\bar{1}0]_\alpha$ direction. This equilibrium shape is expected because the lattice misfit is small in the $\vec{x}$ direction ($-2.1\,\%$), but much larger in the $\vec{y}$ direction ($19.9\,\%$). This elongated shape helps reduce the energy cost of the coherency strain. On the other hand, the slight anisotropy of the interface energy predicted by our EAM potential (*cf* Tab. III) should favor a different equilibrium shape, where the largest facets would be the ones for an interface normal $\vec{y} \parallel [01\bar{1}0]_\alpha$. This shows that the elastic energy is more important than the energy cost of the interfaces in the control of the shape, which minimizes the formation energy of coherent precipitates. However, the reduced dimension in the $[01\bar{1}0]_\alpha$ and not in the $[0001]_\alpha$ direction differs from the shape observed in experiments, suggesting that precipitates in experiments are either non-coherent or their shape is not controlled solely by minimizing their formation energy as described in our simulations.

The formation energy of the precipitates is significantly reduced when they become semi-coherent (Fig. 6), in particular with b_y misfit dislocations accommodating the lattice misfit between the β-Nb and α-Zr phases along the $\vec{y}$ direction. With only these b_y misfit dislocations, the maximal reduction in formation energy is observed with 4 dislocations, decreasing the precipitate energy by $85\,\text{meV/Nb}$ atom. Besides reducing the formation energy, these misfit dislocations modify the predicted equilibrium shape of the precipitate, making the precipitates with minimal energy more elongated in the $\vec{y}$ direction as the number of misfit dislocations b_y increases. The corresponding reduced size $\bar{l}_y$ increases from 0.42 to 1.27 as the number of b_y misfit dislocations increases from 0 to 4. Such a variation of the precipitate elongation in the $\vec{y}$ direction with their coherency appears reasonable. When the precipitate are fully coherent, an important eigenstrain ε^β_{yy} is associated with this direction $\vec{y}$. By reducing the precipitate length in this direction, one reduces the elastic energy necessary to

embed the precipitate in the matrix. Introduction of misfit dislocation allows a reduction of this eigenstrain ε^{β}_{yy} and thus of the associated elastic energy, which becomes less dominating in the precipitate formation energy compared to the energy cost associated with the lattice misfit in the other directions and also the cost of the interfaces.

The precipitate formation energy can be further reduced by b_z misfit dislocations accommodating the lattice misfit in the $\vec{z}$ direction (Fig. 7). With 1 or 2 b_z misfit dislocations, an additional reduction of 80 meV/Nb atom is observed. Precipitates with minimal formation energy have at least 1 b_z misfit dislocation and between 3 and 5 b_y misfit dislocations, leading to precipitates shapes defined by the reduced sizes $1.1 \leq \bar{l}_x \leq 1.8$, $1 \leq \bar{l}_y \leq 1.5$ and $0.5 \leq \bar{l}_z \leq 1$. These precipitates have similar sizes in the $\vec{x}$ and $\vec{y}$ directions and a reduced size in the $\vec{z} \parallel [0001]_\alpha$ direction. This shape agrees with the experimental observations where precipitates appear as platelets lying in the basal planes of the α-Zr matrix. High resolution TEM observations (HREM) [8, 23] have shown that misfit dislocations are present at the interfaces between the β-Nb precipitates and the α-matrix.

The reduction of lattice misfit between the precipitate and the matrix due to misfit dislocations significantly impacts the precipitate formation energy and equilibrium shape. This is illustrated by plotting the precipitate formation energy as a function of the misfit strain defined by Eq. 2 (Fig. 8). It is evident that the formation energy is minimal when enough misfit dislocations are present at the interfaces to cancel the lattice misfit between the precipitate and the matrix, *i.e.* when the misfit strain ε_{uu} is close to zero. This is true both for $\vec{y}$ and $\vec{z}$ directions. Although these misfit dislocations increase the cost of the interfaces, which become incoherent, the reduction in lattice misfit, and hence the associated elastic energy, is more significant, ultimately leading to lower formation energies. To go further in the analysis and understand how interface energies vary with the coherency state, it would be possible to use the same approach as in section III to calculate the energy of semi-coherent interfaces, either *ab initio* or with the EAM potential, by varying the number of α-Zr and β-Nb planes at the interface.

4D-STEM [23] has shown that the spacing between $(0001)_\alpha$ planes in the matrix around the precipitates does not exhibit significant tensile strain, *i.e.* $\varepsilon_{zz} \simeq 0$ with our choice of orientation. This is consistent with our analysis, indicating that precipitates are semi-coherent with enough misfit dislocations to cancel the lattice mismatch between both phases and minimize their energy. Although the same [23], and other [8], TEM observations have

clearly identified the presence of such misfit dislocations at the precipitate/matrix interfaces, it cannot be excluded that other physical mechanisms, particularly variations in chemical composition of the precipitates and the matrix near the interface, also contribute to the reduction of the lattice misfit. However, the reduction in misfit and the associated elastic energy appears to be a strong driving force for the precipitate shape.

V. CONCLUSIONS

Atomistic simulations performed with a Zr-Nb potential reveal that the formation energy of β-Nb precipitates, which appear under irradiation in α-Zr, significantly decreases when the precipitates become semi-coherent. The energy is minimal when enough misfit dislocations are present at the interface to cancel the lattice misfit between the α-Zr and β-Nb phases. The shape of fully coherent precipitate that minimizes the formation energy does not match the experimental observations. However, the most stable semi-coherent precipitates are platelets lying in the basal planes of the hcp lattice, with a reduced size along the $[0001]_\alpha$ direction, in perfect agreement with the shapes observed in experiments. Therefore, atomistic simulations suggest that β-Nb particles formed under irradiation are not fully coherent to minimize their energy, explaining the presence of misfit dislocations seen by TEM at their interface [8, 23].

The newly developed Zr-Nb EAM potential used in these simulations appears well-suited for studying Nb precipitates in zirconium. It incorporates all the necessary physical ingredients to model coherency strain and the associated energy cost between the β-Nb precipitates and α-Zr matrix. Comparison with *ab initio* calculations shows that it also gives a reasonable description of the interfaces between both phases. This potential offers a promising route to study at the atomic scale, the impact of β-Nb precipitates, particularly their interactions with gliding dislocations, and gain insights into their hardening contribution.

In our simulations, we have assumed that the β precipitates and the α matrix are pure Nb and Zr phases. However, experiments have shown that native β-Nb precipitates have a Nb composition that decreases with the irradiation dose. Secondary nano-precipitates appearing under irradiation have a lower Nb concentration than predicted by thermodynamic equilibrium between bulk phases, typically only between 60 and 75 % Nb for particles created by neutron irradiation [15, 22, 55], or even less, around 40 % Nb for proton irradiation [9].

Such deviations from equilibrium compositions offer an alternative way to reduce the lattice misfit between α-Zr and β-Nb phases, thereby decreasing the elastic energy arising from coherency constraints. β-Nb needles are also enriched in Fe [9] compared to the surrounding solid solution, which should also impact the lattice misfit with the α-matrix. Using the same EAM potential, future works can extend this study to investigate how deviations from perfect stoichiometry affect the precipitate structure and energy, considering both misfit dislocations and composition variations. It will also be possible to go beyond the static simulations at 0 K performed in the present work. One expects a dependence to temperature of the precipitate formation energy through a variation with temperature of both the elastic constants and the interface energies. But the most important impact would probably be the varying lattice misfits because of the different thermal expansions of the β-Nb and α-Zr phases, as well as the anisotropic expansion of α-Zr.

The coherency between the matrix and precipitates affects the precipitates sink strength [56]. It appears reasonable to assume that β-Nb precipitates are coherent, when they start to appear. Because of the smallest atomic volume of the β phase compared to the α phase, they create a tensile stress field around them in the α matrix, thus leading to an attractive elastic interaction with interstitial atoms and a repulsion with vacancies. Coherent β-Nb precipitates should therefore be biased, absorbing more interstitials than vacancies. These unbalanced fluxes of point-defects should rapidly result in the coherency loss of the β-Nb precipitates, with semi-coherent precipitates being more stable than coherent ones as seen in our atomistic simulations. Once the net flux of absorbed interstitials allows for compensation of the lattice misfit between the α-Zr and β-Nb phases, the stress field around these semi-coherent precipitates becomes small and precipitates are expected to act as unbiased sinks, eliminating both vacancies and interstitials created by irradiation equally. By promoting point-defects recombination without creating unbalanced fluxes between vacancies and interstitials, their effect should be beneficial, slowing down the evolution of the irradiation-induced microstructure.

Appendix A: EAM potential

We use the EAM formalism to describe atomic interactions. The energy of a system containing N atoms at positions $\vec{r}_i$ is given by

$$E(\vec{r}_1, \ldots, \vec{r}_N) = \sum_{i=1}^{N} \left[F_{X_i}(\bar{\rho}_i) + \frac{1}{2} \sum_{j \neq i} \phi_{X_i X_j}(r_{ij}) \right],$$

with $r_{ij} = \|\vec{r}_j - \vec{r}_i\|$ is the distance between atoms i and j. X_i is the type of atom, either Zr or Nb, located at site i. $\phi_{X_i X_j}(r)$ is the pair interaction between atoms of types X_i and X_j. $F_{X_i}(\bar{\rho}_i)$ is the embedding function of atom type X_i calculated for the density $\bar{\rho}_i$ existing at site i. This density is obtained by summing the contributions of neighboring atoms,

$$\bar{\rho}_i = \sum_{j \neq i} \rho_{X_j}(r_{ij}),$$

where $\rho_{X_j}(r)$ is the elemental density of atom type X_j.

For Zr, we use the EAM potential developed by Mendelev and Ackland, specifically the potential noted #3 in Ref. [34]. We only fit the functions describing pure Nb interactions *i.e.* $F_{\mathrm{Nb}}(\rho)$, $\rho_{\mathrm{Nb}}(r)$ and $\phi_{\mathrm{NbNb}}(r)$, as well as the cross pair interaction $\phi_{\mathrm{ZrNb}}(r)$ between Zr and Nb atoms. The functions $F_{\mathrm{Zr}}(\rho)$, $\rho_{\mathrm{Zr}}(r)$ and $\phi_{\mathrm{ZrZr}}(r)$ are directly taken from Ref. [34]. Before combining them with the Nb part, we rescale this Zr EAM potential. The description given by an EAM potential for a pure element X is indeed not altered by the following changes [57]:

$$\begin{aligned} \rho_X(r) &= \rho^0_X(r)/A_X, \\ F_X(\rho) &= F^0_X(A_X\,\rho) - B_X\,\rho, \\ \phi_{XX}(r) &= \phi^0_{XX}(r) + 2B_X\,\rho^0_X(r)/A_X, \end{aligned}$$

where $\rho^0_{\mathrm{X}}(r)$, $\phi^0_{\mathrm{XX}}(r)$ and $F^0_{\mathrm{X}}(\rho)$ are the original functions. The original Zr EAM #3 potential is rescaled with the parameters $A_{\mathrm{Zr}} = 83.3046$ and $B_{\mathrm{Zr}} = -4.08009$.

The Nb embedding function takes different forms for low and high density:

$$\begin{aligned} F_{\mathrm{Nb}}(\rho) &= -a_0\sqrt{\rho} + a_1\,\rho + a_2\,\rho^2 + a_4\,\rho^4, \quad \rho \leq \rho_{\max} \\ &= b_0 + b_1\,(\rho - \rho_{\max}) + (\rho - \rho_{\max})^2\left(b_2 + b_3\,\rho + b_4\,\rho^2\right), \quad \rho \geq \rho_{\max} \end{aligned} \tag{A1}$$

with $b_0 = F_{\mathrm{Nb}}(\rho_{\max})$ and $b_1 = F'_{\mathrm{Nb}}(\rho_{\max})$ to ensure continuity of the embedding function $F_{\mathrm{Nb}}(\rho)$ and its first derivative $F'_{\mathrm{Nb}}(\rho)$ at the density $\rho_{\max}$.

TABLE IV. Parameters defining the pure Nb part and the alloying part of the Zr-Nb EAM potential. Distances r_k are given in Å and the resulting functions F_{Nb}, ϕ_{NbNb} and ϕ_{ZrNb} are expressed in eV.

$F_{\mathrm{Nb}}(\rho)$	$\rho_{\mathrm{Nb}}(r)$	$\phi_{\mathrm{NbNb}}(r)$	$\phi_{\mathrm{ZrNb}}(r)$
$a_0 = 0.216161$	$r_1 = 2.1$	$r_1 = 2.7$ $\phi_1 = -5.32781$	$r_1 = 2.7$ $\phi_1 = 2.95338$
$a_1 = -18.8405$	$r_2 = 2.9$	$r_2 = 2.9$ $\phi_2 = 31.1461$	$r_2 = 2.9$ $\phi_2 = -3.14252$
$a_2 = 1.68589$	$r_3 = 3.8$	$r_3 = 3.0$ $\phi_3 = -0.639147$	$r_3 = 3.0$ $\phi_3 = 2.01447$
$a_4 = -0.0390124$	$r_4 = 4.7$	$r_4 = 3.3$ $\phi_4 = -1.09298$	$r_4 = 3.3$ $\phi_4 = -0.113563$
$b_0 = -41.0077$	$r_5 = 5.8$	$r_5 = 3.6$ $\phi_5 = 0.692798$	$r_5 = 3.6$ $\phi_5 = 0.527162$
$b_1 = -12.8739$	$\rho_1 = -1.91229$	$r_6 = 3.8$ $\phi_6 = 0.973560$	$r_6 = 3.8$ $\phi_6 = 0.0348147$
$b_2 = 73.7419$	$\rho_2 = 0.931266$	$r_7 = 4.2$ $\phi_7 = 4.07840$	$r_7 = 4.2$ $\phi_7 = 0.555228$
$b_3 = -54.2121$	$\rho_3 = 0.0804986$	$r_8 = 4.4$ $\phi_8 = -4.01382$	$r_8 = 4.4$ $\phi_8 = -0.923716$
$b_4 = 9.96109$	$\rho_4 = -0.0364943$	$r_9 = 4.6$ $\phi_9 = 1.98924$	$r_9 = 4.6$ $\phi_9 = 0.770526$
$\rho_{\max} = 2.7$	$\rho_5 = 0.0120155$	$r_{10} = 4.7$ $\phi_{10} = -1.16498$	$r_{10} = 4.8$ $\phi_{10} = -0.279592$
		$r_{11} = 4.8$ $\phi_{11} = -1.09682$	$r_{11} = 5.2$ $\phi_{11} = -0.249193$
		$r_{12} = 5.2$ $\phi_{12} = 0.539737$	$r_{12} = 5.6$ $\phi_{12} = 0.403934$
		$r_{13} = 5.6$ $\phi_{13} = -0.332176$	$r_{13} = 6.0$ $\phi_{13} = -0.127217$
		$r_{14} = 5.8$ $\phi_{14} = 0.651207$	
		$r_{15} = 6.0$ $\phi_{15} = -0.141713$	

The Nb density function is written as a cubic-spline:

$$\rho_{\mathrm{Nb}} = \sum_{k=1}^{5} \rho_k \left(r_k - r\right)^3 H(r_k - r), \tag{A2}$$

where $H(x)$ is the Heaviside function, equal to 0 if $x < 0$ and 1 if $x > 0$.

The Nb-Nb and Zr-Nb pair functions are also written as cubic-splines:

$$\phi_{XY}(r) = \sum_{k=1}^{K} \phi_k \left(r_k - r\right)^3 H(r'_k - r), \tag{A3}$$

with $K = 15$ and 13 for Nb-Nb and Zr-Nb interactions, respectively.

All parameters describing the fitted functions are given in table IV. Cutoff radius of the pair and density functions correspond to the position of the last knot of the cubic-spline, *i.e.* 5.8 Å for $\rho_{\mathrm{Nb}}(r)$ and 6.0 Å for $\phi_{\mathrm{ZrNb}}(r)$ and $\phi_{\mathrm{NbNb}}(r)$.

Appendix B: Infinite interface and elastic energy

We consider a system composed of two phases, α and β, joined at a plane interface with a normal corresponding to the vector $\vec{e}_3$ of the Cartesian axis. A homogeneous pre-strain, ε^α and ε^β, is imposed on each phase to obtain a coherent interface (step 2 in Fig. 1). This pre-strain generates a polarization stress homogeneous in each phase, $\tau^\alpha_{ij} = \lambda^\alpha_{ijkl}\varepsilon^\alpha_{kl}$ and $\tau^\beta_{ij} = \lambda^\beta_{ijkl}\varepsilon^\beta_{kl}$, where λ^α and λ^β are the elastic tensors of each phase in the reference frame of the interface.

An additional homogeneous strain increment $\delta\varepsilon^\alpha$ and $\delta\varepsilon^\beta$, imposed on each phase of the slab system, leads to the variation of the elastic energy with respect to the pre-strained initial state

$$\Delta E(\delta\varepsilon^\alpha, \delta\varepsilon^\beta) = N^\alpha\Omega^\alpha_0\left[\tau^\alpha_{ij}\delta\varepsilon^\alpha_{ij} + \frac{1}{2}\lambda^\alpha_{ijkl}\delta\varepsilon^\alpha_{ij}\delta\varepsilon^\alpha_{kl}\right] + N^\beta\Omega^\beta_0\left[\tau^\beta_{ij}\delta\varepsilon^\beta_{ij} + \frac{1}{2}\lambda^\beta_{ijkl}\delta\varepsilon^\beta_{ij}\delta\varepsilon^\beta_{kl}\right],$$

where N^α and N^β are the number of atoms in each phase and Ω^α_0 and Ω^β_0 their equilibrium atomic volumes. To maintain interface coherency, the components $\delta\varepsilon_{11}$, $\delta\varepsilon_{22}$, and $\delta\varepsilon_{12}$ must be the same in both phases, while the components $\delta\varepsilon_{33}$, $\delta\varepsilon_{13}$, and $\delta\varepsilon_{23}$ can vary independently in each phase.

Minimizing the elastic energy leads to the equilibrium conditions:

$$\begin{gathered}
N^\alpha\Omega^\alpha_0\left[\tau^\alpha_{ij} + \lambda^\alpha_{ijkl}\delta\varepsilon^\alpha_{kl}\right] + N^\beta\Omega^\beta_0\left[\tau^\beta_{ij} + \lambda^\beta_{ijkl}\delta\varepsilon^\beta_{kl}\right] = 0, \text{ for } ij \in \{11, 22, 12\} \\
N^\alpha\Omega^\alpha_0\left[\tau^\alpha_{ij} + \lambda^\alpha_{ijkl}\delta\varepsilon^\alpha_{kl}\right] = 0, \text{ for } ij \in \{33, 13, 23\} \\
N^\beta\Omega^\beta_0\left[\tau^\beta_{ij} + \lambda^\beta_{ijkl}\delta\varepsilon^\beta_{kl}\right] = 0, \text{ for } ij \in \{33, 13, 23\}
\end{gathered}$$

We can choose the pre-strains ε^α and ε^β such that the strain increments $\delta\varepsilon^\alpha$ and $\delta\varepsilon^\beta$ fulfilling these equilibrium conditions are null. This corresponds to an initially pre-strained state where the average stress is zero. Replacing polarization stresses with their expressions, we obtain:

$$\begin{gathered}
N^\alpha\Omega^\alpha_0\lambda^\alpha_{ijkl}\varepsilon^\alpha_{kl} + N^\beta\Omega^\beta_0\lambda^\beta_{ijkl}\varepsilon^\beta_{kl} = 0, \text{ for } ij \in \{11, 22, 12\} \\
N^\alpha\Omega^\alpha_0\lambda^\alpha_{ijkl}\varepsilon^\alpha_{kl} = 0, \text{ for } ij \in \{33, 13, 23\} \\
N^\beta\Omega^\beta_0\lambda^\beta_{ijkl}\varepsilon^\beta_{kl} = 0, \text{ for } ij \in \{33, 13, 23\}.
\end{gathered}$$

This set of 9 equations is completed by the coherency conditions at the interface. Considering that the phase α have orthogonal periodicity vectors $l^\alpha_1\vec{e}_1$ and $l^\alpha_2\vec{e}_2$ which match the

periodicity vectors $l_1^\beta \vec{e}_1$ and $l_2^\beta \vec{e}_2$ of the β phase in the interface plane, the three following equations are obtained:

$$\begin{aligned}
\left(1+\varepsilon_{11}^\alpha\right) l_1^\alpha &= \left(1+\varepsilon_{11}^\beta\right) l_1^\beta \\
\left(1+\varepsilon_{22}^\alpha\right) l_2^\alpha &= \left(1+\varepsilon_{22}^\beta\right) l_2^\beta \\
\varepsilon_{12}^\alpha &= \varepsilon_{12}^\beta
\end{aligned}$$

The strains in each phase, ε^α and ε^β, are finally obtained by inverting this system of 12 equations.

ACKNOWLEDGMENTS

This work was performed using HPC resources from GENCI-IDRIS and -TGCC (Grants 2022-096847) and was funded by the project PRECCI from the French nuclear tripartite institute (EDF, CEA, Framatome).

[1] C. Lemaignan, Zirconium alloys: Properties and characteristics, in *Comprehensive Nuclear Materials*, edited by R. J. M. Konings, T. R. Allen, R. E. Stoller, and S. Yamanaka (Elsevier, 2012) Chap. 2.07, pp. 217–232.

[2] A. T. Motta and D. R. Olander, *Light water reactor materials* (American Nuclear Society, La Grange Park, Illinois, 2017).

[3] A. F. Guillermet, Thermodynamic analysis of stable phases in the Zr-Nb system and calculation of the phase diagram, Z. Metallkd. **82**, 478 (1991).

[4] P. Lafaye, C. Toffolon-Masclet, J.-C. Crivello, and J.-M. Joubert, Experimental investigations and thermodynamic modelling of the Cr–Nb–Sn–Zr system, Calphad **64**, 43 (2019).

[5] M. Cottura and E. Clouet, Solubility in Zr-Nb alloys from first-principles, Acta Mater. **144**, 21 (2018).

[6] V. N. Shishov, A. V. Nikulina, V. A. Markelov, M. M. Peregud, A. V. Kozlov, S. A. Averin, S. A. Kolbenkov, and A. E. Novoselov, Influence of neutron irradiation on dislocation structure and phase composition of Zr-base alloys, in *Zirconium in the Nuclear Industry: Eleventh*

International Symposium (ASTM International, 100 Barr Harbor Drive, PO Box C700, West Conshohocken, PA 19428-2959, 1996) pp. 603–622.

[7] G. Yuan, L. Zhang, Q. Yue, H. Gu, G. Li, and J. Shen, Microstructural characteristics of β precipitates in Zr–1Nb alloy, Mater. Chem. Phys. **165**, 87 (2015).

[8] J. Ribis, S. Doriot, and F. Onimus, Shape, orientation relationships and interface structure of beta-Nb nano-particles in neutron irradiated zirconium alloy, J. Nucl. Mater. **511**, 18 (2018).

[9] Z. Yu, A. Couet, and M. Bachhav, Irradiation-induced Nb redistribution of ZrNb alloy: An APT study, J. Nucl. Mater. **516**, 100 (2019).

[10] Y. Matsukawa, I. Okuma, H. Muta, Y. Shinohara, R. Suzue, H. Yang, T. Maruyama, T. Toyama, J. Shen, Y. Li, Y. Satoh, S. Yamanaka, and H. Abe, Crystallographic analysis on atomic-plane parallelisms between bcc precipitates and hcp matrix in recrystallized Zr-2.5Nb alloys, Acta Mater. **126**, 86 (2017).

[11] H. Yang, Y. Matsukawa, S. Kano, Z. Duan, K. Murakami, and H. Abe, Investigation on microstructural evolution and hardening mechanism in dilute Zr-Nb binary alloys, J. Nucl. Mater. **481**, 117 (2016).

[12] Y. Matsukawa, H. Yang, K. Saito, Y. Murakami, T. Maruyama, T. Iwai, K. Murakami, Y. Shinohara, T. Kido, T. Toyama, Z. Zhao, Y. Li, S. Kano, Y. Satoh, Y. Nagai, and H. Abe, The effect of crystallographic mismatch on the obstacle strength of second phase precipitate particles in dispersion strengthening: bcc Nb particles and nanometric Nb clusters embedded in hcp Zr, Acta Mater. **102**, 323 (2016).

[13] R. W. Gilbert, K. Farrell, and C. E. Coleman, Damage structure in zirconium alloys neutron irradiated at 573 to 923 K, J. Nucl. Mater. **84**, 137 (1979).

[14] V. Perovic, A. Perovic, G. C. Weatherly, L. M. Brown, G. R. Purdy, R. G. Fleck, and R. A. Holt, Microstructural and microchemical studies of Zr-2.5Nb pressure tube alloy, J. Nucl. Mater. **205**, 251 (1993).

[15] S. Doriot, B. Verhaeghe, J.-L. Béchade, D. Menut, D. Gilbon, J.-P. Mardon, J.-M. Cloué, A. Miquet, and L. Legras, Microstructural evolution of M5TM alloy irradiated in PWRs up to high fluences - comparison with other Zr base alloys, in *Zirconium in the nuclear industry: 17$^{\text{th}}$ international symposium*, American Society for Testing and Materials Special Technical Publication, Vol. 1543, edited by R. Comstock and P. Barbéris (American Society Testing and Materials, W Conshohocken, USA, 2013) pp. 759–799, symposium: B10 17th International

Symposium on "Zirconium in the Nuclear Industry", February 03-07, 2013, Taj Krishna, Hyderabad, India.

[16] F. Onimus, S. Doriot, and J.-L. Béchade, Radiation effects in zirconium alloys, in *Comprehensive Nuclear Materials*, edited by R. J. Konings and R. E. Stoller (Elsevier, 2020) Chap. 3.01, pp. 1–56, 2nd ed.

[17] S. Adisa, J. Hu, and M. Swenson, APT characterization and modeling of irradiation-induced Nb-rich nanoclustering in Zr-1.0%Nb alloys, Materialia **16**, 101040 (2021).

[18] Z. Yu, J. W. Werden, N. A. Capps, K. D. Linton, and A. Couet, (S)TEM/EDS study of native precipitates and irradiation induced Nb-rich platelets in high-burnup M5®, J. Nucl. Mater. **544**, 152667 (2021).

[19] B. Jenkins, J. Haley, M. Moody, J. Hyde, and C. Grovenor, Apt and tem study of behaviour of alloying elements in neutron-irradiated zirconium-based alloys, Scripta Materialia **208**, 114323 (2022).

[20] J. Ribis, F. Onimus, J.-L. Béchade, S. Doriot, A. Barbu, C. Cappelaere, and C. Lemaignan, Experimental study and numerical modelling of the irradiation damage recovery in zirconium alloys, J. Nucl. Mater. **403**, 135 (2010).

[21] F. Onimus, S. Doriot, A. Ambard, F. Bourlier, B. Verhaeghe, T. Le Jolu, and C. Cappelaere, Understanding post-irradiation creep behavior of $M5_{framatome}$ zirconium alloy, J. Nucl. Mater. **597**, 155138 (2024).

[22] Z. Yu, M. Bachhav, F. Teng, L. He, M. Dubey, and A. Couet, STEM/EDS and APT study on the microstructure and microchemistry of neutron irradiated ZIRLO^{TM}, J. Nucl. Mater. **573**, 154139 (2023).

[23] Z. Yu, C. Zhang, P. M. Voyles, L. He, X. Liu, K. Nygren, and A. Couet, Microstructure and microchemistry study of irradiation-induced precipitates in proton irradiated ZrNb alloys, Acta Mater. **178**, 228 (2019).

[24] C. Cann, C. So, R. Styles, and C. Coleman, Precipitation in Zr-2.5Nb enhanced by proton irradiation, J. Nucl. Mater. **205**, 267 (1993).

[25] E. Francis, R. P. Babu, A. Harte, T. Martin, P. Frankel, D. Jädernäs, J. Romero, L. Hallstadius, P. Bagot, M. Moody, and M. Preuss, Effect of Nb and Fe on damage evolution in a Zr-alloy during proton and neutron irradiation, Acta Mater. **165**, 603 (2019).

[26] M. Topping, A. Harte, T. Ungár, C. P. Race, S. Dumbill, P. Frankel, and M. Preuss, The effect of irradiation temperature on damage structures in proton-irradiated zirconium alloys, J. Nucl. Mater. **514**, 358 (2019).

[27] O. T. Woo, R. M. Hutcheon, and C. E. Coleman, Precipitation in Zr-2.5Nb during 10 MeV electron irradiation, MRS Proc. **373**, 189 (1994).

[28] A. Sarce, Stability of precipitates in the anisotropic α-Zr matrix under irradiation, J. Nucl. Mater. **185**, 214 (1991).

[29] A. Sarce, Stability of β-85 wt% Nb precipitates in pressure tubes, J. Nucl. Mater. **208**, 300 (1994).

[30] A. Sarce, Precipitate morphologies predicted using discrete lattice descriptions, J. Nucl. Mater. **232**, 152 (1996).

[31] U. Dahmen, Orientation relationships in precipitation systems, Acta Metall. **30**, 63 (1982).

[32] G. Kresse and J. Furthmüller, Efficiency of ab-initio total energy calculations for metals and semiconductors using a plane-wave basis set, Comput. Mater. Sci. **6**, 15 (1996).

[33] J. P. Perdew, K. Burke, and M. Ernzerhof, Generalized gradient approximation made simple, Phys. Rev. Lett. **77**, 3865 (1996).

[34] M. I. Mendelev and G. J. Ackland, Development of an interatomic potential for the simulation of phase transformations in zirconium, Philos. Mag. Lett. **87**, 349 (2007).

[35] C. Kittel, *Introduction to Solid State Physics:*, 7th ed. (Wiley, New York, 1996).

[36] P. Villars and L. D. Calvert, *Pearson's Handbook of Crystallographic Data for Intermetallic Phases* (American Society for Metals, Materials Park, OH, USA, 1985).

[37] E. S. Fisher and C. J. Renken, Single-crystal moduli and the hcp $\rightarrow$ bcc transformation in Ti, Zr and Hf, Phys. Rev. **135**, A482 (1964).

[38] R. Roberge, Lattice parameter of niobium between 4.2 and 300 K, J. Less Common Met. **40**, 161 (1975).

[39] K. J. Carroll, Elastic constants of niobium from 4.2 to 300K, J. Appl. Phys. **36**, 3689 (1965).

[40] K. Maier, M. Peo, B. Saile, H. E. Schaefer, and A. Seeger, High–temperature positron annihilation and vacancy formation in refractory metals, Philos. Mag. A **40**, 701 (1979).

[41] M. R. Fellinger, H. Park, and J. W. Wilkins, Force-matched embedded-atom method potential for niobium, Phys. Rev. B **81**, 144119 (2010).

[42] J. Behler, Perspective: Machine learning potentials for atomistic simulations, The Journal of Chemical Physics **145**, 10.1063/1.4966192 (2016).

[43] A. M. Goryaeva, J.-B. Maillet, and M.-C. Marinica, Towards better efficiency of interatomic linear machine learning potentials, Comput. Mater. Sci. **166**, 200 (2019).

[44] M. Liyanage, D. Reith, V. Eyert, and W. A. Curtin, Machine learning for metallurgy V: A neural-network potential for zirconium, Phys. Rev. Materials **6**, 063804 (2022).

[45] Y. Luo, J. A. Meziere, G. D. Samolyuk, G. L. W. Hart, M. R. Daymond, and L. K. Béland, A set of moment tensor potentials for zirconium with increasing complexity, J. Chem. Theory Comput. **19**, 6848 (2023).

[46] E. Clouet, Screw dislocation in zirconium: An ab initio study, Phys. Rev. B **86**, 144104 (2012).

[47] N. Chaari, E. Clouet, and D. Rodney, First-principles study of secondary slip in zirconium, Phys. Rev. Lett. **112**, 075504 (2014).

[48] N. Chaari, E. Clouet, and D. Rodney, First order pyramidal slip of $1/3\ \langle 1\bar{2}10\rangle$ screw dislocations in zirconium, Metall. Mater. Trans. A **45**, 5898 (2014).

[49] Émile Maras and E. Clouet, Secondary slip of screw dislocations in zirconium, Acta Mater **223**, 117398 (2022).

[50] M.-C. Marinica, L. Ventelon, M. R. Gilbert, L. Proville, S. L. Dudarev, J. Marian, G. Bencteux, and F. Willaime, Interatomic potentials for modelling radiation defects and dislocations in tungsten, J. Phys.: Condens. Matter **25**, 395502 (2013).

[51] V. Vitek, Intrinsic stacking faults in body-centred cubic crystals, Philos. Mag. **18**, 773 (1968).

[52] V. Vitek and V. Paidar, Non-planar dislocation cores: A ubiquitous phenomenon affecting mechanical properties of crystalline materials, in *Dislocations in Solids*, Vol. 14, edited by J. P. Hirth (Elsevier, 2008) Chap. 87, pp. 439–514.

[53] Y. Mishin, Atomistic modeling of the γ and γ'-phases of the Ni–Al system, Acta Mater. **52**, 1451 (2004).

[54] L. Thuinet and R. Besson, Ab initio study of competitive hydride formation in zirconium alloys, Intermetallics **20**, 24 (2012).

[55] J.-L. Béchade, D. Menut, S. Doriot, S. Schlutig, and B. Sitaud, X-ray diffraction analysis of secondary phases in zirconium alloys before and after neutron irradiation at the MARS synchrotron radiation beamline, J. Nucl. Mater. **437**, 365 (2013).

[56] G. S. Was, *Fundamentals of Radiation Materials Science* (Springer New York, 2017).

[57] A. Caro, D. A. Crowson, and M. Caro, Classical many-body potential for concentrated alloys and the inversion of order in iron-chromium alloys, Phys. Rev. Lett. **95**, 075702 (2005).